[Article ID] 1003－6326(2002)06－1063－06

Effects of temperature boundary conditions on equiaxed dendritic growth in phase-field simulations of binary alloy①

YU Yan-mei(于艳梅), YANG Gen-cang(杨根仓), ZHAO Da-wen(赵达文), LU Yi-li(吕衣礼)
(State Key Laboratory of Solidification Processing,
Northwestern Polytechnical University, Xi′an 710072, China)

[Abstract] By the phase-field approach, the dendritic growth in binary alloy melt was simulated respectively using two types of temperature boundary conditions, i.e., the constant temperature boundary by which the boundary temperature was fixed at the initial temperature, and Zero-Neumann temperature boundary. The influences of the temperature boundary conditions on numerical results are investigated. How to choose appropriate temperature boundary conditions is proposed. The results show that: 1) when the computation region is limited to a changeless size, the Zero-Neumann and constant temperature boundary conditions lead to the different dendritic growth behaviors, and the Zero-Neumann condition is preferable to the constant temperature condition; 2) when the computation region is enlarged continually with the computational time according to the increasing thermal diffusion scale, the two types of temperature boundary conditions achieve the consistent tip velocities and tip radii, and they both are appropriate choices.

[Key words] phase-field approach; temperature boundary condition; thermal diffusion
[CLC number] TG 248; TG 244 **[Document code]** A

1 INTRODUCTION

Phase-field method is very powerful in simulation of dendritic growth, and is becoming one of the important ways to achieve the industrial prediction of the solidification microstructure[1~4]. In past, the phase-field simulation is conducted on the isothermal condition where the temperature of melt is considered to be constant during the computation[5~7]. However, the latent heat released during solidification must change the thermal regime in melt[8], even for metals, and affect the final microstructure. Hence, the non-isothermal phase-field simulation of binary alloy is necessary to predict exactly solidification microstructure of alloys. In the non-isothermal simulation, the effects of the temperature boundary condition on dendritic growth have to be clarified firstly. In the paper, the dendritic growth of binary alloy is simulated under the two types of temperature boundary, Zero-Neumann temperature boundary condition, and constant temperature boundary condition, to investigate influences of temperature boundary conditions on the simulated results. Then, based on the simulated results, how to choose the appropriate temperature boundary condition is proposed.

2 MATHEMATICAL MODEL AND NUMERICAL ISSUES

We derive the phase-field model of binary alloy starting from an entropy formulation[9] that is written as

$$S=\int_{\Omega}\left[s(\Phi,c,e)+\frac{1}{2}\varepsilon^2(\nabla\Phi)^2+\frac{1}{2}\delta^2(\nabla c)^2\right]\mathrm{d}\Omega \tag{1}$$

where s is entropy density, Φ, phase-field variable, c, concentration of solute B in solvent A, e, internal density, ε and δ are coefficients which account for the phase-field and concentration gradient term corrections respectively, Ω, the region occupied by the system.

The evolution of phase-field is given by

$$\frac{\mathrm{d}\Phi}{\mathrm{d}t}=M_{\Phi}\frac{\delta S}{\delta\Phi} \tag{2}$$

Conservation laws govern the solute and energy density transport:

$$\frac{\mathrm{d}c}{\mathrm{d}t}=-\nabla\cdot M_c\nabla\frac{\delta S}{\delta c} \tag{3}$$

$$\frac{\mathrm{d}e}{\mathrm{d}t}=-\nabla\cdot M_e\nabla\frac{\delta S}{\delta e} \tag{4}$$

where M_{Φ}, M_c, M_e are parameters related to the interfacial mobility, solute and thermal diffusion, respectively.

In the above equations, the variational derivatives are given by

$$\frac{\delta S}{\delta\Phi}=\frac{\partial s}{\partial\Phi}+\nabla\cdot\varepsilon^2\nabla\Phi \tag{5}$$

$$\frac{\delta S}{\delta c}=\frac{\partial s}{\partial c}+\nabla\cdot\delta^2\nabla\Phi \tag{6}$$

$$\frac{\delta S}{\delta e}=\frac{\partial s}{\partial e}=\frac{1}{T} \tag{7}$$

The free energy of the system is given by

① [Foundation item] Project(59971037) supported by the National Natural Science Foundation of China and Doctoral Dissertation Innovation Foundation of Northwestern Polytechnical University [Received date] 2001－12－17; [Accepted date] 2002－03－05

$$f(\Phi, c, T) = (1-c)f_A + cf_B + \frac{RT}{V_m}\ln(1-c) + \ln c \quad (8)$$

where V_m is molar volume, R, ideal gas constant, f_A and f_B are respectively the free energy densities of the pure element A and B. f_A can be written as

$$f_A = TG^A(\Phi) + [e_s^A(T_m^A) - C^A T_m^A + p(\Phi)L^A]\left(1 - \frac{T}{T_m^A}\right) - C^A T\ln\left(\frac{T}{T_m^A}\right) \quad (9)$$

where C^A is specific heat, L^A, latent heat per unit volume. Choosing $G^A(\Phi) = W^A\Phi^2(1-\Phi)^2$ and $p(\Phi) = \Phi^3(10 - 15\Phi + 6\Phi^2)$ indicates that the bulk solid and liquid are described by $\Phi = 0$ and $\Phi = 1$. The free energy f_B has the similar expression with the material parameters labeled with the superscript A replaced with the ones related to the B species.

Using $ds = -\frac{1}{T}df$, taking Eqns. (8), (9) into Eqns. (2) ~ (4), the governing equations of the evolution of phase-field, concentration and thermal field are derived that are written as

$$\frac{d\Phi}{dt} = M_\Phi[\nabla\varepsilon^2\nabla\Phi - Wg'(\Phi) - P'(\Phi)/T\cdot((1-c)H_A + cH_B)] \quad (10)$$

$$\frac{dc}{dt} = -\nabla\cdot(M_c P'(\Phi)(H_A - H_B)\nabla\Phi) + \nabla\cdot\left(\frac{R}{v_M}\frac{1}{c(1-c)}M_c\nabla c\right) - \nabla(M_c\Gamma(\Phi, T)\nabla T - \nabla(M_c\nabla(\delta^2\nabla^2 c)) \quad (11)$$

$$\frac{\partial T}{\partial t} = K\nabla^2 T - \frac{(L_A(1-c) + cL_B)}{c_V}P'(\Phi)\frac{\partial\Phi}{\partial t} - \frac{(L_A - L_B)}{c_V}(1 - P(\Phi))\frac{\partial c}{\partial t} \quad (12)$$

where

$$H_A = L^A\left(\frac{1}{T} - \frac{1}{T_m^A}\right) \quad (13)$$

$$H_B = L^B\left(\frac{1}{T} - \frac{1}{T_m^B}\right) \quad (14)$$

$$\Gamma(\Phi, T) = \nabla\cdot\frac{2P(\Phi)}{T^2}(L^A - L^B) \quad (15)$$

$$M_c = \frac{V_m}{R}(1-c)c(D_s - P(\Phi)D_l) \quad (16)$$

where D_s and D_l are the solute diffusion coefficients in the solid and liquid, respectively.

For simplicity, the approximations are made that $c^A = c^B = c_V$, $W^A = W^B = W$. The equal solid and liquid thermal conductivities K are assumed. M_Φ, W and ε are the phase-field parameters which are related to the physical parameters: interfacial energy σ, kinetic coefficient β, melting point T_M, latent heat L, and interface thickness ξ, as shown in the following:

$$M_\Phi = \frac{T_M^2\beta}{6\sqrt{2}L\xi} \quad (17)$$

$$W = \frac{3\sigma}{\sqrt{2}T_M\xi} \quad (18)$$

$$\varepsilon = \frac{6\sqrt{2}\sigma\xi}{T_M} \quad (19)$$

The interface thickness ξ, as an input parameter, has to be specified firstly, which influences not only the simulation results, but also the computational costs. In this paper, ξ is taken as (50~ 70) d_0 (d_0 is the capillary length), which is small enough to achieve qualitative results.

Eqns. (10) ~ (12) are discretized in space using second order finite difference on uniform Cartesian grids, and in time using first order finite difference approximation. ADI algorithm is applied for the heat equation. The space step is selected as $\Delta x = 0.5\xi$, the time step is specified in such a way that $\Delta t < \Delta x^2/(5D)$ according to $D = D_c$ or $D = M_\Phi\varepsilon^2$ for keeping stable under time-step iterations.

For an initial nucleus of the radius r,

When $x^2 + y^2 \leqslant r^2$,

$$\Phi = 1, T = T_0, c = c_0 \quad (20)$$

When $x^2 + y^2 > r^2$,

$$\Phi = -1, T = T_0, c = c_0 \quad (21)$$

where x and y are the coordinate axes, T_0 is the initial temperature of the undercooled melt, and c_0 is the alloy composition.

The Zero-Neumann boundary conditions for Φ and c are imposed at the boundaries of the computational domain. Two types of temperature boundary conditions are used, viz. the constant temperature condition by which the boundary temperature is fixed at 1 543 K and the Zero-Neumann boundary condition.

A Ni-Cu alloy is chosen for the simulations, where, $c_0 = 0.491\ 1$ and $T_0 = 1\ 543$ K, which indicates the supersaturation is about 0.86 and the undercooling is about 23 K. All phase-field parameters are specified according to the physical properties of the alloy given in Table 1. The magnitude of anisotropy is 0.05. The amplitude of the noise fluctuations is 0.5.

Table 1 Physical data for Ni and Cu[10]

Parameter	Nickel (A)	Copper (B)
T_M/K	1 728	1 358
L/(J·cm^{-3})	2 350	1 728
σ/(J·cm^{-2})	3.7×10^{-5}	2.9×10^{-5}
β/(cm·K^{-1}·s^{-1})	0.33	0.39
D_s/(cm^2·s^{-1})	10^{-9}	
D_l/(cm^2·s^{-1})	10^{-5}	
K/(cm^2·s^{-1})*	0.155	
c_V/(J·K^{-1}·cm^{-3})**	5.0	
V_m	7.4	

* —From data of Conti et al(Ref. [11]); ** —Average value of Ni and Cu.

Five calculations are preformed, and their computational times are equal. First, the isothermal calculation is conducted in a computation region of 1 500 × 1 500 nodes. Then, in the same computation region, two non-isothermal calculations are conducted respectively on the constant temperature boundary condition and Zero-Neumann temperature boundary condition mentioned above. Finally, using the two types of temperature boundary conditions, two non-isothermal calculations are preformed again in a continually extended computation region according to the increasing thermal diffusion field scale. In order to save the computational costs, the computation region is extended only in one direction, and in the other direction, the node number remain unchanged. Therefore, the complete dendrite morphology could not be obtained, but the tip steady state could be achieved.

3 NUMERICAL RESULTS AND DISCUSSION

Figs. 1~ 3 show the isothermal dendrite morphology and non-isothermal ones using two types of temperature boundary conditions in the same computational region. From the figures, we can see that the non-isothermal dendrite pattern under the constant temperature boundary condition is similar to the isothermal dendrite, except that the side-branches is less developed than those of the isothermal dendrite. However, the dendrite obtained on the Zero-Neumann temperature boundary condition has greatly different pattern of no side-branches and much less scale.

The corresponding tip velocities and tip radii of dendrites shown in Figs. 1~ 3 are presented in Figs. 4 and 5. From the figures, it could be found that the tip velocity and the tip radius obtained by the non-isothermal calculation using the constant temperature boundary condition are close to those of isothermal dendrite,

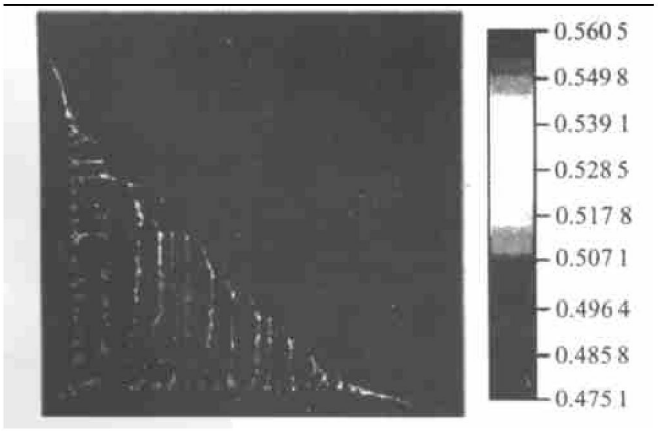

Fig. 1 Dendrite pattern and concentration field of isothermal dendrite
(The scale displayed is 3.75×10^{-3} cm.)

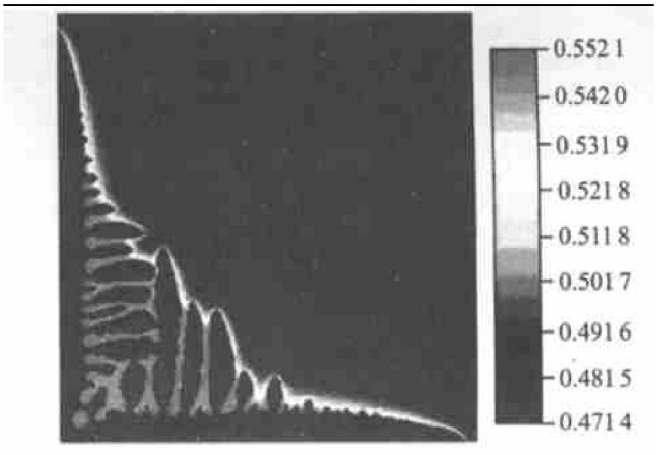

Fig. 2 Dendrite pattern and concentration field of non-isothermal dendrite using constant temperature boundary condition
(The scale displayed is 3.68×10^{-3} cm.)

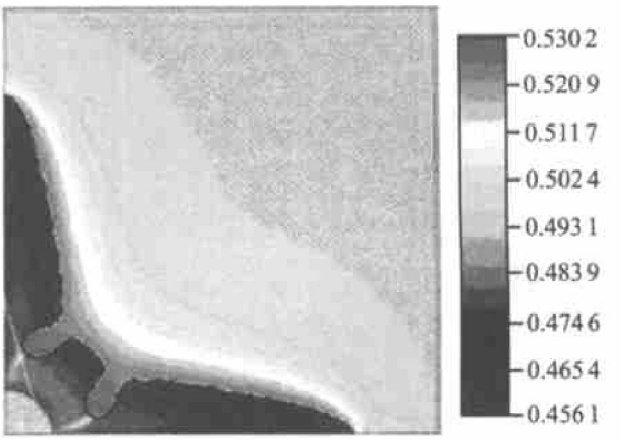

Fig. 3 Dendrite pattern and concentration field of non-isothermal dendrite using Zero-Neumann temperature boundary condition
(The scale displayed is 1.46×10^{-3} cm.)

whereas the dendrite obtained under the Zero-Neumann temperature boundary condition has much less tip velocity and much larger tip radius.

Under the constant temperature boundary condition, the non-isothermal simulation derive the almost same dendrite behavior with that obtained in the isothermal simulation, which indicates the dendrite growth in the undercooled supersaturated binary alloy melt is mainly controlled by solute diffusion, whereas under Zero-Neumann temperature boundary condition, the greatly different simulation results indicates that the dendrite growth is governed by thermal diffusion. The two self-contradictory conclusions result from the two different temperature boundary conditions.

Under the Zero-Neumann boundary condition, the latent heat is accumulated in the computational box. Therefore, the temperature of the melt rises up and tends

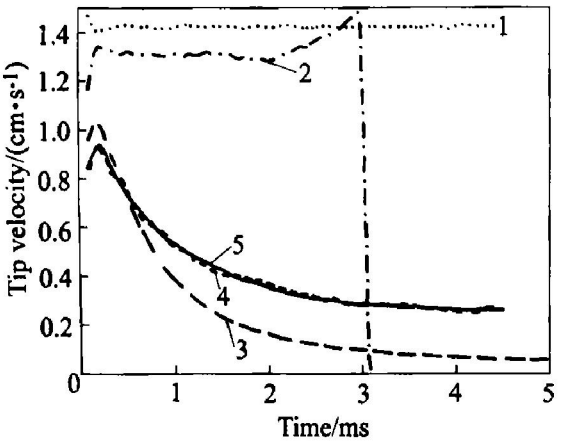

Fig. 4 Tip velocity versus time under different conditions

1 —Isothermal calculation on 1 500 × 1 500 grids;
2 and 3 —Norr isothermal calculation on 1 500 × 1 500 grids using the constant temperature and Zero-Neumann temperature boundary condition respectively;
4 and 5 —Norr isothermal calculation on continually extended computation region using constant temperature and Zero-Neumann boundary condition respectively

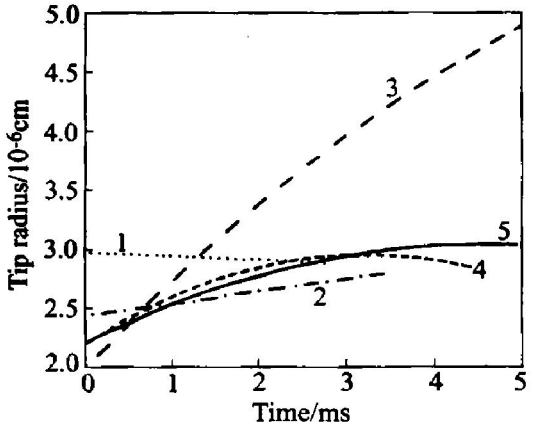

Fig. 5 Tip radius versus time under different conditions

1 —Isothermal calculation on 1 500 × 1 500 grids;
2 and 3 —Norr isothermal calculation on 1 500 × 1 500 grids nstant temperature and Zero-Neumann temperature boundary condition respectively;
4 and 5 —Norr isothermal calculation on a continually extended computation region using the constant temperature and Zero-Neumann boundary condition respectively

to be uniform, and the initial undercooling and the spatial temperature gradient become decreasing, which leads to the decaying dendritic growth velocity shown by the solid line in Fig. 4. Fig. 6 presents the temperature profiles in the melt under the Zero-Neumann temperature boundary condition (plotted by the solid circle). In Fig. 6, the temperature of the melt all ascends to about 1 552 K from the initial temperature 1 543 K, and the tip temperature gradient is about 0.002 7 K/m.

But for the constant temperature boundary, despite

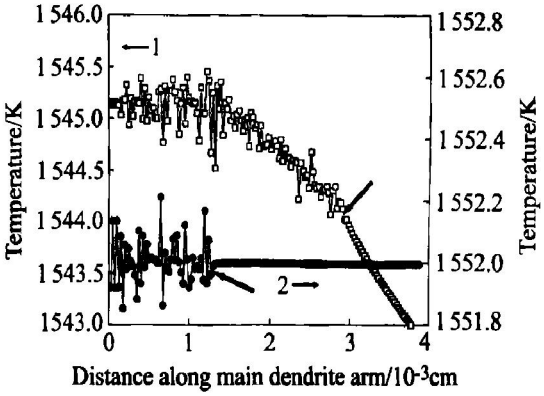

Fig. 6 Thermal regimes under different temperature boundary conditions

(The solid arrows point out the location of the dendrite tip.)

1 —Boundary temperature fixed at 1 543 K;
2 —Zero-Neumann condition

that the temperature of the internal melt rises up gradually due to the latent heat built up in the interdendritic regions, the temperature on the boundary remains at 1 543 K. Therefore the spatial temperature gradient is kept well in the melt. As shown in Fig. 6, the tip temperature gradient is 1.19×10^5 K/m, much larger than the one under the Zero-Neumann boundary condition, which is the reason why the tip velocity under the constant temperature boundary condition is greatly larger than that under the Zero-Neumann boundary condition.

Furthermore, the constant temperature boundary also causes the increasing tip temperature gradient when the dendrite is reaching the edge of the computation box illustrated in Fig. 7, which causes the increasing tip velocity shown by the dash dotted

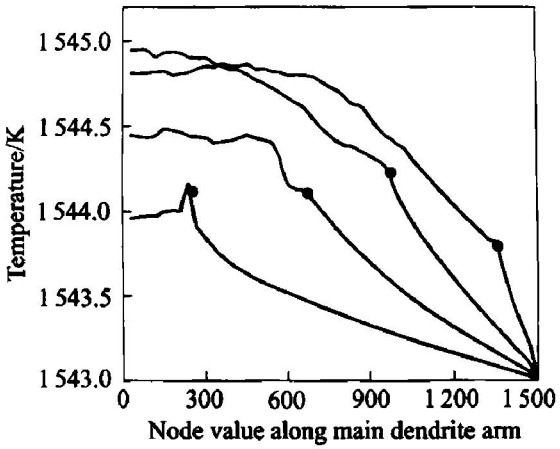

Fig. 7 Temperature profiles at four different times under constant temperature boundary condition

(From the left to right, the times are 4.0×10^{-3}, 1.2×10^{-2}, 2.0×10^{-2}, and 2.8×10^{-2} s, respectively. Solid dots superimposed on the curves mark the location of the corresponding dendrite tips.)

line in Fig. 4. Therefore using the constant temperature boundary condition, the increasing dendritic growth is obtained instead of the decaying growth obtained under the Zero-Neumann condition.

The equiaxed dendritic growth in castings has shown that when the diffusion region of a dendrite increases to a certain size, the transfer of heat and solute will be baffled by the diffusion fields of the neighboring dendrites, and the dendritic growth will slow down gradually and enter into the ripening stage. If the domain boundaries are viewed as a surface midway between adjacent nuclei, the course can be simulated through limiting the size of the computational domain[10], just like the simulations we have preformed above. The simulation under the Zero-Neumann temperature boundary condition emerges nicely the course. However, the simulated results obtained under the constant temperature boundary condition indicate that the dendrite would grow faster and faster when the solidification front approaches the boundary, and no ripening would take place, which is apparently in contradiction with the real behaviors of the equiaxed dendritic growth. So, we can conclude that the constant temperature boundary condition is used incorrectly here; the similar dendrite patterns, tip velocity and radius with the isothermal dendrite are the outcome of the inappropriate temperature boundary condition. Therefore, the conclusion[12] that the dendritic growth in the undercooled supersaturated binary alloy melt is mainly controlled by solute diffusion needs much inspection.

The constant temperature condition equals a temperature boundary condition of a time varying finite heat flux at the boundary acting to cool the box. In the recent phase-field simulations, the size of the computation box is usually less than 100 μm. For so small box, the cooling velocity is demanded to be larger than 10^6 K/s to keep the constant initial undercooling at the boundary. But, as a matter of fact so large cooling velocity is impossible in real system. Hence, in the phase-field simulation, for a computational region of a finite size, it's preferable to adopt the Zero-Neumann temperature boundary condition rather than the constant temperature boundary condition.

In order to obtain the tip steady state, it is necessary to avoid the influence of the computation box, which can be realized through extending continually the computation region according to the increasing thermal diffusion scale. Using the two types of temperature boundary conditions, two non-isothermal computations also are conducted in a computational domain that is extended continually with the computational time according to the increasing thermal diffusion scale. The tip velocity and the tip radius are derived, as shown by the solid line and short dash line in Figs. 4 and 5. From the figures, it could be found two kinds of temperature boundary conditions achieve almost the identical relationships of the tip velocity and the tip radius with time. The dendrite tip decays with the time and enters into the steady state through a transient stage, at the same time, the tip radius increases with time and tends to converge. The variation rule of the tip velocity and the tip radius versus time is the same as that obtained using the Zero-Neumann boundary in the computation region of 1 500 × 1 500 grids, but the convergent tip velocity is larger than the latter, the tip radius is just on the contrary.

Because the size of the computation region is enlarged continually according to the increasing thermal diffusion scale, the computation region is always large enough to diffuse completely heat. The heat flux on the boundary is always zero, and at the same time, the boundary temperature remains at the initial temperature. Therefore, the Zero-Neumann condition and the constant temperature condition both correctly characterized the temperature boundary condition on the boundary of the computation region. So, they both are appropriate if the non-isothermal simulation is preformed on a computational region of the increasing size.

It needs to be noted that the suggestion we proposed about how to determine the temperature boundary condition in this paper is based on the fact that the phase-field method only can deal with a single dendrite in the undercooled melt because the scale it can simulate is limited by the computation ability recently. If the simulating scale is improved to be a magnitude of centimetre or larger so that the solidifying process of a sample can be handled in the future, the temperature boundary condition should be determined according to the specific process.

4 CONCLUSIONS

1) In the phase-field simulations of non-isothermal binary dendritic growth, different temperature boundary conditions lead to different dendrite growth behaviors.

2) When the computation region is limited to an unchanged size, the Zero-Neumann temperature boundary condition leads to a decaying dendritic growth, whereas the constant temperature boundary condition leads to an increasing dendritic growth. The former is consistent with the real equiaxed dendritic growth in castings, but the latter is in contradiction with it. In this case, the Zero-Neumann condition is preferable to the constant temperature condition.

3) When the computation region is enlarged continually with the computational time according to the increasing thermal diffusion scale, the Zero-Neumann and the constant temperature boundary conditions achieve the consistent tip velocities and tip radii. In this case, two types of temperature boundary conditions both are appropriate.

[REFERENCES]

[1] Collins J B, Levin H. Diffuse interface model of diffusion-limited crystal growth [J]. Phys Rev B, 1985, 31(9): 6119-6122.

[2] Caginalp G, Fife P C. Phase field methods for interfacial boundaries [J]. Phys Rev B, 1986, 33(11): 7792-7794.

[3] Conti M. Growth of a needle crystal from an undercooled alloy melt [J]. Phys Rev E, 1997, 56(3): 3197-3202.

[4] ZHENG Cai-xing, LIU Rang-su, DONG Ke-jun, et al. Simulation study on transition mechanisms of microstructures during forming processes of amorphous metals [J]. Trans Nonferrous Met Soc China, 2001, 11(1): 35-39.

[5] Warren J A, Boettinger W J. Prediction of dendritic growth and microsegregation patterns in a binary alloy using the phase-field method [J]. Phys Rev A, 1991, 43(10): 1310-1317.

[6] Wheeler A A, Murray B T, Schaefer R J. Computation of dendrites using a phase field model [J]. Phys D, 1993, 66(10): 243-262.

[7] Boettinger W J, Wheeler A A, Murray B T. Prediction of solute trapping at high solidification rates using a diffuse interface phase field theory of alloy solidification [J]. Mater Sci Eng, 1994, A178(10): 217-223.

[8] Karma A, Sarkissian A. Interface dynamics and banding in rapid solidification [J]. Phys Rev E, 1993, 47(4): 513-533.

[9] Wang S L, Skerka R F. Thermodynamically-consistent phase-field models for solidification [J]. Physica D, 1993, 69: 189-200.

[10] Boetinger W J, Warren J A. The phase-field method: simulation of alloy dendritic solidification during recalescence [J]. Metall Mater Trans A, 1996, 27A(3): 657-669.

[11] Conti M. Solidification of binary alloys: thermal effects studied with the phase field model [J]. Phys Rev E, 1997, 55(1): 765-771.

[12] Loginova I, Amberg G, Agren J. Phase-field simulations of non-isothermal binary alloy solidification [J]. Acta Mater, 2001, 49: 573-581.

(Edited by PENG Chao-qun)